Fanara *et al.*
Low-carbon Materials and Green Construction (2026) 4:9
https://doi.org/10.1007/s44242-026-00105-0

Low-carbon Materials
and Green Construction

ORIGINAL ARTICLE Open Access

Application of a hysteresis model for the water retention curve in recycled aggregates concrete: experimental and numerical FE^2 approaches

Arthur Fanara[1,2*], Luc Courard[1†] and Frédéric Collin[1†]

Abstract

Water retention curves are used to describe the degree of water saturation in porous materials. These curves exhibit hysteresis, meaning that the relationship between water content and applied suction depends on the wetting and drying history of the material and environmental conditions. This study investigates the effect of hysteresis on the durability of concrete made from recycled concrete aggregates (RCA), demonstrating that the Van Genuchten model can be applied to such recycled materials. A chemo-hydraulic, multiscale finite element squared (FE^2) model was developed and validated. This model represents chloride ingress within the unsaturated porous structure of concrete. The constitutive equations are formulated at the mortar scale based on experimentally measured intrinsic material properties. Through numerical homogenization, these properties are upscaled to simulate the macroscopic behavior of concrete made with 100% RCA. Hysteresis calibration properties were also obtained experimentally. Experimental validation confirms that the Van Genuchten model can be applied to recycled aggregate concrete. A sensitivity analysis of the hysteresis model parameters revealed that water content is significantly impacted. However, this influence is less pronounced when studying chloride ingress.

Keywords Hysteresis, Durability, Finite element analysis, Multiscale modeling, Recycled aggregates, Transport properties

1 Introduction

The construction industry is one of the most important industry worldwide, and is the most energy-consuming industry, particularly due to the production of concrete and other cement-based materials. In 2019, the estimated production of concrete reached 1.2 billion tons in the EU-27 [1, 2], which required an enormous amount of aggregates, mostly naturally, extracted from quarries: 2.55 billion tons were extracted in the same year for the EU-27, 45% of that volume being destined for concrete [2, 3]. In the mean time, a significant amount of construction and demolition wastes is generated. In 2021 for the EU-27, it accounted for 36% of the global waste stream, which represents around 800 million tons, excavated soils included [2, 4]. This stream is also expected to continuously increase as the existing building environment ages.

Despite the environmental impacts associated with concrete production and waste management, the incorporation of recycled materials is increasingly encouraged as an alternative to natural resources. In this context, recycled concrete aggregates (RCA) have been investigated for many years as a means to decrease the demand for natural

†Luc Courard and Frédéric Collin contributed equally to this work.

*Correspondence:
Arthur Fanara
arthur.fanara@uliege.be
[1] Urban and Environmental Engineering, University of Liège, Allée de la Découverte, 4000 Liège, Belgium
[2] FNRS-F.R.I.A., Fonds de la Recherche Scientifique, Rue d'Egmont 5, 1000 Bruxelles, Belgium

aggregates. However, their use often leads to reduced durability performance, primarily due to alterations in the material's porous structure [5–7]. These changes in pore structure directly affect the water transport behavior of concrete. Consequently, a detailed assessment of water transfer properties is required to better understand how such substitution influences overall durability [6].

While speaking of durability of concrete, it may be defined as its ability to withstand the effects of both time and degradation processes, while retaining its initial design properties [8]. Degradation mechanisms in concrete arise from various sources, including freeze–thaw cycles, carbonation, chloride ingress, or, more commonly, a combination of these [9, 10]. Most deterioration processes are strongly influenced by the water content within the concrete's pore network. During freeze–thaw cycles, higher degrees of saturation generally intensify damage. In the case of chloride penetration and carbonation, aggressive ions rely on the presence of moisture to migrate toward and interact with the steel reinforcement [11]. Moreover, corrosion reactions tend to be most severe when the degree of water saturation approaches approximately 85% [12]. A comprehensive understanding of water transport in concrete is therefore essential for reliably assessing its durability.

The water content of numerous geomaterials, including concrete, has been widely characterized in the literature using water retention curves (WRC) [6, 13–17]. The WRC describe the relationship between the saturation degree of a porous medium and its boundary environmental conditions, typically relative humidity and temperature, through the concept of total suction. Total suction is commonly expressed using the law of Kelvin:

$$s = -\rho_w \frac{R\,T}{M_w} \ln(RH) \tag{1}$$

with the total suction s (Pa), the density of water ρ_w (kg/m^3), the constant of perfect gases R (8.314 3 (J/(K.mol))), the molar mass of water M_w (18.016 (g/mol)), the temperature T (K) and relative humidity RH. Throughout this study, the total suction is assumed equal to the matrix suction, thereby neglecting the effects of the osmotic contribution. The matrix suction is defined as the pressure differential between the air and the water pressures:

$$s = P_g - P_w \tag{2}$$

where the gas and water pressures are noted P_g and P_w (Pa), respectively. This hypothesis is only valid for solutions whose ionic concentration is close to zero, that is deionized or slightly ionized water. In the case of sea water, the osmotic pressure may reach approximately −2.97 MPa, which is rather negligible compared to atmospheric suction that may reach −59.3 MPa (which is equivalent to a temperature and relative humidity of 273.4 K and 62.5%, respectively).

For this definition to hold, the porous network of concrete is treated within the framework of porous media theory, where pores contain only air (gas or dissolved), water (liquid or vapor), or mixtures of these. Water saturated media contain only liquid water and dissolved gas, whereas unsaturated media contain both water and air. Mixture theory [18, 19] is also adopted, allowing all phases to coexist within the same spatial domain and enabling separate mass-balance formulations for each phase [18] while accounting for their interactions [19].

The shape of the WRC is strongly controlled by the pore structure of the material [15, 20], and typically spans saturated, funicular, pendular, and residual regimes [15, 20, 21]. Porous materials such as concrete also exhibit distinct drying and wetting retention curves, whose similar functional forms bound an infinite set of intermediate scanning paths governed by hydraulic history [15]. This hysteresis arises from several mechanisms: the ink-bottle effect, linked to irregular pore geometries [13, 17, 20, 22, 23]; differences between advancing and receding contact angles (raindrop effect) [13, 17, 20, 22, 23]; and air entrapment during rewetting, which can represent up to 10% of pore volume [17, 20, 22–25]. As shown in Fig. 1, the boundary drying and wetting curves define outer limits that are not crossed, while any number of scanning curves may form between them [13, 23].

Numerous models have been proposed to describe the WRC of geomaterials, broadly classified as physically based (domain) models [26] and empirical models [17, 24]. Domain models represent the porous system as a collection of idealized pore domains, typically assuming that each pore is either full or empty, and are primarily applied to soils or natural aggregates [17, 24]. While they provide insight into pore-scale processes, they do not capture the complex heterogeneity introduced by recycled aggregates and the adherent mortar in recycled aggregate concrete (RAC). Empirical models, such as the Van Genuchten formulation adopted here [27], rely on fitted functional relationships to experimental data and offer flexibility [17, 21, 27], but they generally lack physical consistency in representing hysteresis and do not explicitly account for the mesoscale structure of RAC. Two subgroups are commonly identified [17]: models that apply the same equation to both boundary curves with different fitting parameters [27], and models that explicitly relate drying and wetting curves.

Concrete structures are continuously exposed to fluctuating environmental conditions, which induce

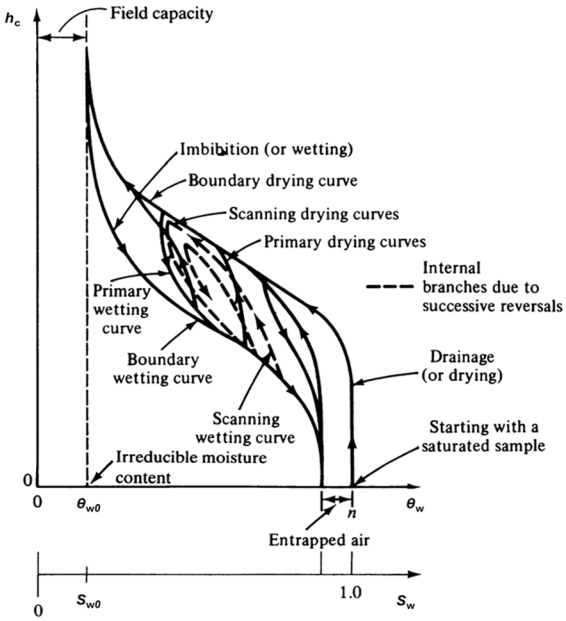

Fig. 1 Hysteresis in the water retention curve (from [13]). The *x*-axis represents the water saturation degree S_W, while the *y*-axis represents the suction through the capillary pressure head h_c

significant variations in their degree of saturation. Although water retention hysteresis plays a key role in these processes, it is still commonly neglected in numerical modeling of concrete. This omission is mainly due to the lack of experimental datasets required for model calibration, and to the increased number of parameters introduced when hysteresis is incorporated. As a result, no consensus currently exists regarding how hysteresis should be represented in numerical models of unsaturated concrete [24], particularly for RAC, whose pore structure is more complex.

Furthermore, studies specifically addressing water retention curves at the scale of RAC remain very limited. Most existing work on recycled materials focuses primarily on the properties of the aggregates themselves rather than on the behavior of the composite concrete. For instance, Jiménez et al. (2014) [28] investigated the water retention curve behavior of recycled aggregates derived from demolition waste. However, the impact of these aggregate-level properties on the hydraulic behavior of concrete incorporating recycled aggregates has not been comprehensively explored. Other studies have examined the water retention properties of cementitious materials [29], but these investigations considered only natural aggregates, without addressing the complexity of RAC.

This study addresses this gap by providing an integrated experimental and numerical framework that enables the reliable incorporation of water retention hysteresis into multiscale models for chloride ingress in RAC. We experimentally determined the full set of WRC parameters, including those governing hysteresis, and used them to implement a hysteretic WRC within a finite element squared (FE^2) multiscale chloride transport model. The results demonstrate that accounting for hysteresis significantly improves the prediction of saturation evolution and chloride penetration, offering new insights into the durability of concrete made with recycled aggregates.

2 Materials and methods

2.1 Materials

The experimental part of this work consisted of the determination of the intrinsic properties of both water and chlorides transfer inside several cement-based materials:

- The first material is the reference concrete, which is made with natural aggregates (NA) and named NAC. The cement used is CEM I 42.5 N, along with 0/2 Rhine sand and 2/7 natural limestone aggregates;
- The second material is a RAC whose composition is identical to the reference material except for the natural aggregates that have been substituted with RCA. Those RCA were obtained in another study from the University of Liège, SeRaMCo, by crushing multiple times, with an impact crusher, sandstone concrete blocks previously cast in our laboratory [30]. Their particle size distribution (PSD) was reconstructed to be identical to the PSD of the natural aggregates, and the full substitution is done in volume. The RCA have been characterized prior to the mixing: their mean porosity is equal to 17.49% in volume, and their mean cement content, measured by salicylic acid dissolution, is equal to 10.98 % in mass [31];
- The third and last material is an equivalent mortar, named E-M. It was composed through the concrete equivalent mortar (CEM) method [32], and used the same Rhine sand and cement as the two other materials. It was proved experimentally that its transport properties are similar to the ones of the bulk mortar that may be found in the two concretes.

Table 1 details the quantities of each ingredients in the three materials presented above. More details are available in Fanara et al. [33]. The PSDs of the NA and RCA are presented in Fig. 2. The initial PSDs are shown, as well as the final PSD of the RCA which was corrected to be identical to the one of the NA.

Table 1 Quantities of cement, water, sand, natural and recycled concrete aggregates used for each cement-based material investigated in this study. The total w/c accounts for water adsorption by the aggregates, whereas the effective w/c is corrected to exclude this effect. Although our recycled aggregates were pre-saturated with the additional water required for the RAC mix, the effective w/c of the concrete remains unchanged

Material	Cement (kg/m^3)	Water (kg/m^3)	Rhine sand (kg/m^3)	Natural agg. (kg/m^3)	Recycled agg. (kg/m^3)	w/c	w/c_{eff}
NAC	320	172.5	643	1 111	-	0.54	0.50
RAC	320	201.2	643	-	946	0.63	0.50
E-M	622.5	336.0	1 337	-	-	0.54	0.54

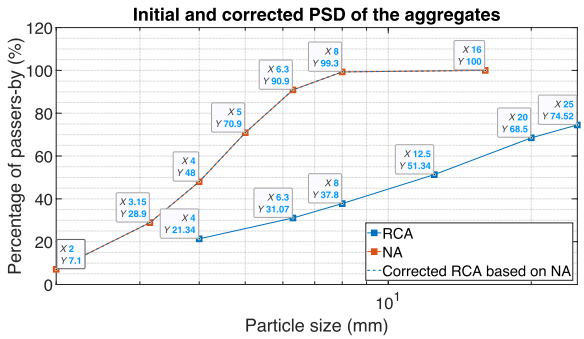

Fig. 2 Initial particle size distribution of the natural and recycled concrete aggregates, and corrected particle size distribution for the RCA used in the mix, corrected to be identical to the one of the natural aggregates

2.2 Methods

The experimental program was designed to characterize both moisture-related transport mechanisms and chloride migration behavior. It comprised two main categories of tests:

- **Water transport characterization** [6]:
  - Dry and saturated bulk densities, water absorption, as well as open porosity accessible to water, were measured in accordance with ASTM C 642-97, *Standard Test Method for Density, Absorption, and Voids in Hardened Concrete*;
  - The intrinsic permeability to water was evaluated following the procedure specified in the standard NBN EN ISO 17892−11: 2019, which describes laboratory methods for determining water permeability of soils and geomaterials [34];
  - The water retention behavior was determined using the vapor equilibrium technique, as described in Sect. 2.2.1.
- **Chloride transport characterization** [33]:
  - The apparent chloride diffusion coefficient D_{app} was assessed under non-steady-state diffusion conditions, in accordance with NBN EN 12390−11, *Testing hardened concrete - Part 11: Determination of the chloride resistance of concrete by unidirectional diffusion* [35].

2.2.1 Static sorption and desorption

The water retention curve is commonly described by adjusting an empirical relationship to experimental data, such as the model proposed by Van Genuchten [27]. From an experimental standpoint, the degree of water saturation of a porous material can be related to suction via Kelvin's law (Eq. 1). In the present work, the main drying and wetting curves were determined using the vapor control technique [36]. This approach relies on the assumption that hygroscopic materials exchange water vapor with the surrounding air until thermodynamic equilibrium is reached, meaning that vapor pressure and temperature are identical inside and outside the pore network [36]. By regulating the ambient relative humidity with saturated salt solutions and maintaining a constant temperature using a climatic chamber, a series of (s; S_r) data points can be obtained along the water retention curves [16, 37]. The saline solutions employed in this study, together with their corresponding target suctions at 21°C, are listed in Table 2.

Square specimens with dimensions of 100 × 100 × 10 mm^3 (five samples per material) were first conditioned to either a fully saturated state or oven-dried at 105 °C until a stable mass was reached. The specimens were then transferred to sealed chambers containing one of the selected saline solutions. At weekly intervals, the specimen mass was recorded together with the ambient air conditions, namely relative humidity and temperature. After a conditioning period of approximately three

Table 2 Saline solutions and their corresponding target RH (%) and suction (MPa) at 21 °C, employed to determine the WRC properties of the investigated materials

Saline solution	Silica salt	$MgCl_2$	$Ca(NO_3)_2$	NaCl	KCl
Target RH (%)	6	35	56	75	90
Target suction (MPa)	−381	−142.5	−78.7	−39.1	−14.3

months, the mass variation fell below 1% per month, at which point hygroscopic equilibrium was assumed to be achieved. The degree of water saturation was subsequently calculated by comparing the equilibrium mass with previously determined dry and saturated masses.

To capture hysteresis effects, the specimens were sequentially exposed to different humidity environments: after reaching equilibrium and recording the corresponding mass in one chamber, the samples were relocated to another chamber with a different relative humidity. This procedure was repeated several times, allowing the drying and wetting paths to be clearly distinguished.

3 Numerical multiscale FE^2 model

The numerical framework employed in this study is a multiscale, multiphase approach based on the FE^2 methodology. It has been introduced in the finite element software LAGAMINE [38], initially developed at the University of Liège.

This model enables the simulation of coupled water and gas transport, as well as chloride ion diffusion and advection, within both saturated and unsaturated porous media. At the subscale, the representative volume element (RVE) consists of a concrete slice comprising mortar, either newly cast or the existing adhered mortar in RCA, and impermeable NA, as illustrated in Fig. 3.

Previous studies have demonstrated that this approach can accurately reproduce experimental behavior of concrete by applying numerical homogenization to mortar intrinsic properties [39].

FE^2 multiscale modeling generally follows a four-step work-flow. First, the structural domain is meshed, and each Gauss point of the macroscale model is associated with a mesoscale RVE, such as the one shown in Fig. 3. This mesoscale description captures the heterogeneities of concrete. In our case, the RVE explicitly represents new and old mortar phases as well as impervious aggregates, so that the macroscopic behavior of concrete emerges directly from the intrinsic properties of its mortar components.

Since water, gas and chloride transfer are investigated, the key material parameters used at the mesoscale (listed in Table 3) are the porosity of the mortar phases, their intrinsic water permeability, the parameters of their water retention curves, and their chloride diffusion coefficients.

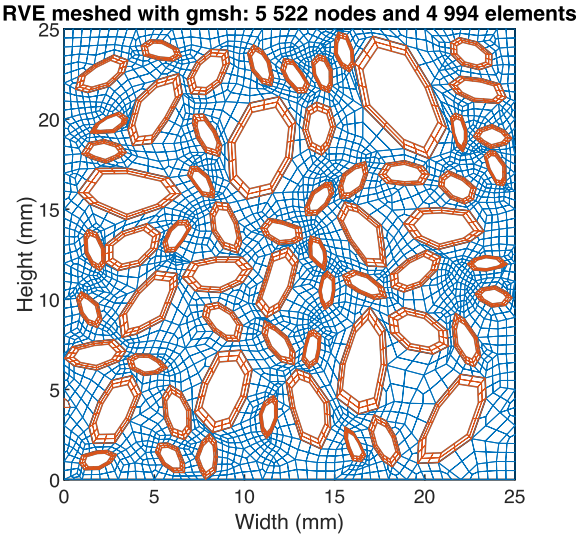

Fig. 3 Illustration of a subscale used for the multiscale numerical modeling of our RAC. The new mortar is shown in blue, while the adhered mortar is depicted in orange. Each mortar phase can exhibit different transport properties. The natural aggregates, assumed impermeable relative to the mortar, are left unmeshed. The RVE has a surface fraction of mortar equal to 61.1%, meanwhile our experimental concrete had a volume fraction of mortar equal to 58.9%. Because the model is two-dimensional, aggregates exhibit a cylindrical shape, which is a strong hypothesis that was taken into account by reverse modeling of experimental results

Based on the boundary conditions applied at the macroscale, that is water and gas pressure, which control the suction, and chloride content, corresponding periodic boundary conditions are imposed on the RVE. It is done by calculating the macroscopic variation of the boundary condition at the specific Gauss point's location. The calculated averaged value and gradients are then translated to the corners of the RVE, and serve as mesoscale boundary conditions [40–42]. The finite element resolution at the mesoscale then provides the local water, gas and chloride fluxes. These are finally homogenized, through the calculation of averaged flows and storage terms over the surface of the elements of the RVE, and fed to the macroscale so that each macroscale Gauss point is assigned a single set of effective transport properties [40, 43, 44]. This homogenization step is central to the model, as it enables the durability performance of concrete to be predicted solely from the intrinsic properties of mortar.

A summary of theses four steps is represented in Fig. 4.

More details about this model are available in Fanara et al. [39]. Some constitutive equations have evolved since, and the new ones are presented hereafter. The parameters employed in the developed model were all determined through the experimental work, and are visible in Table 3.

3.1 Constitutive equations

The FE^2 model developed accounts for multiphasic flows in porous recycled concrete, under the hypothesis of an isothermal medium. Two phases are defined through the theory of mixture presented previously:

- A liquid phase in which dissolved air is inside liquid water;
- A gas phase in which water vapor and dry air are mixed.

Several transport mechanisms are therefore to be defined, for each species:

- Advection flow of the liquid water;
- Advection and diffusion flows of the dissolved air;
- Advection and diffusion flows of the water vapor;
- Advection and diffusion flows of the gaseous air.

3.1.1 Mesoscale liquid and gas flows

The mass balance equations of water and air inside the porous matrix of concrete, in a fixed and underformable system, under the hypothesis of steady-state, are:

$$\frac{\partial}{\partial x_j}\left(\rho_w^l\, v_j^l + \rho_w^g\, v_j^g\right) + \frac{\partial}{\partial x_j}\left(i_j^{w,g}\right) = 0 \tag{3}$$

$$\frac{\partial}{\partial x_j}\left(\rho_a^g\, v_j^g + \rho_a^l\, v_j^l\right) + \frac{\partial}{\partial x_j}\left(i_j^{a,d} + i_j^{a,g}\right) = 0 \tag{4}$$

The first term of each equation is the mass flow by advection, v_j (m/s) being the mean velocity of the phase, and the second term is the mass flow by diffusion, i_j (m/s) being the diffusive flow. In Eq. 3, $\rho_w^l\, v_j^l$ is the advective flow of liquid water, $\rho_w^g\, v_j^g$ is the advective flow of water vapor, and $i_j^{w,g}$ is the diffusive flow of water vapor. In Eq. 4, $\rho_a^g\, v_j^g$ is the advective flow of gaseous air, $\rho_a^l\, v_j^l$ is the advective flow of dissolved air, $i_j^{a,d}$ is the diffusive flow of dissolved air, and $i_j^{a,g}$ is the diffusive flow of gaseous air.

First, let us review the advective flows for both Eqs. 3 and 4. The first term of the advective flow of liquid water is the water density, which varies with the mean water pressure:

$$\rho_w^l = \rho_{w,0} \times \left(1 + \frac{P_{w,average} - P_{w,0}}{\chi_w}\right) \tag{5}$$

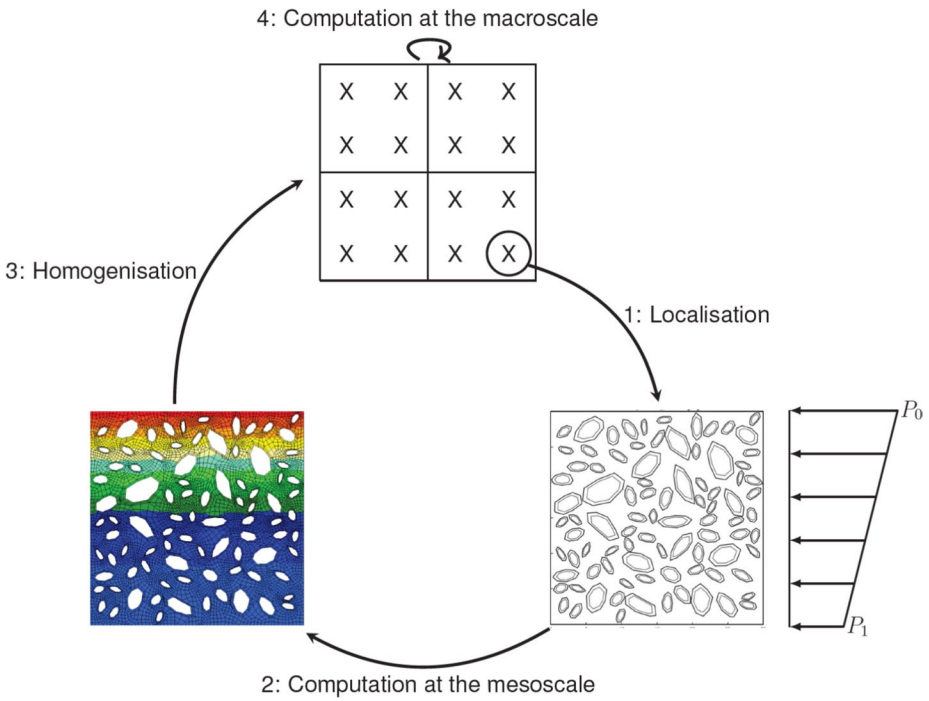

Fig. 4 Conceptual representation of the FE^2 modeling work-flow and its four iterative steps performed on each Gauss point of the macroscale during the multiscale computation

where $\rho_{w,0}$ (kg/m^3) is the initial density of liquid water, $P_{w,average}$ (Pa) is the mean pressure at the macroscale integration point, and $P_{w,0}$ (Pa) is the initial pressure inside the porous structure (pressure at which $\rho_{w,0}$ was calculated). This relation is also dependent on the fluid compressibility, noted χ_w (Pa^{-1}) (at 20 °C, $1/\chi_w = 5 \times 10^{-10}$ Pa^{-1}). The water density may also vary depending on the ionic concentration of chlorides, but it has been neglected at this stage, its influence being deemed less important than that of the water pressure.

Darcy's law is used to describe the movement of liquid phase inside the porous medium. Under the hypothesis of a homogeneously permeable medium, the fluid velocity is:

$$v_j^l = -\frac{k_{int}\ k_{rel,w}}{\mu^w}\left(\frac{\partial P_w}{\partial\ x_j} + \rho_w\ g_j\right) \tag{6}$$

where k_{int} (m^2) is the intrinsic permeability of the porous matrix, $k_{rel,w}$ is the water relative permeability, μ^w (Pa.s) is the dynamic viscosity of water, $(\partial P_w)/(\partial x_j)$ is the gradient of water pressure, and g_j (m/s^2) is the gravity term along the j direction.

The relative permeability $k_{rel,w}$ varies along with the water saturation degree: it is (theoretically) equal to 0 in perfectly dry conditions, or equal to 1 in saturated conditions. The model used to express this relation is the empirical model of Van Genuchten [27]:

$$k_{rel,w} = \sqrt{S_{r,w}} \times \left(1 - \left(1 - S_{r,w}^{1/m_{VG}}\right)^{m_{VG}}\right)^2 \tag{7}$$

where $S_{r,w}$ is the degree of saturation in liquid water of the porous medium and m_{VG} is a model parameter associated to the curvature of the water retention curve [6].

To obtain the advective flow of water vapour, one requires the density of water vapour ρ_w^g [kg/m^3], which is obtained through the law of perfect gases. The density of the gas mix is indeed the sum of the density of the dry air and the water vapour:

$$\rho^g = \rho_a^g + \rho_w^g \quad \text{with} \quad P_{gas}^g = \frac{\rho_{gas}^g}{M_{gas}}\ R\ T \tag{8}$$

$$\longrightarrow \rho_w^g = \rho_{w,0}^g\ \exp\left(\frac{(P_w - P_g)M_w}{\rho_w\ R\ T}\right) \tag{9}$$

where $\rho_{w,0}^g$ (kg/m^3) is the density of saturating water vapour:

$$\rho_{w,0}^g = [194.4\ \exp(-0.06373 \times (T - 273) + (0.1634 \times 10^{-3}(T - 273)^2)\Big]^{-1} \tag{10}$$

Darcy's law is also used to describe the movement of gaseous air inside the porous medium. Under the same assumptions as for the liquid water, the gas flux writes:

$$v_j^g = -\frac{k_{int}\ k_{rel,g}}{\mu^g}\left(\frac{\partial P_g}{\partial\ x_j} + \rho_g g_j\right) \tag{11}$$

$k_{rel,g}$ is the gas relative permeability, μ^g (Pa.s) is the dynamic viscosity of the gaseous mix, and $(\partial P_g)/(\partial x_i)$ is the gradient of gas pressure. Based on the porous media theory, the addition of the degree of saturation of liquid water and that of gaseous air must be equal to one [27], yielding the gas relative permeability:

$$k_{rel,g} = \sqrt{1 - S_{r,w}} \times \left(1 - S_{r,w}^{1/m_{VG}}\right)^{2\ m_{VG}} \tag{12}$$

The dynamic viscosity of the gaseous mix, used in Eq. 11, is given by the following equation:

$$\mu^g = \left[\frac{X_a^g}{\mu_a^g} + \frac{X_w^g}{\mu_w^g}\right]^{-1} \quad \text{where} \quad X_{a/w}^g = \frac{\rho_{a/w}^g}{\rho^g} \tag{13}$$

with μ^g the gas dynamic viscosity and X^g its mass fraction. The Kelvin law is used to express a thermodynamic equilibrium between the two phases of water: liquid water and water vapour. It defines the pressure of water vapour, noted P_w^g, as a function of the suction, written s:

$$P_w^g = P_w^{g,0}\ \exp\left(\frac{-s\ M_w}{R\ T\ \rho_w}\right) \tag{14}$$

with $P_w^{g,0}$ (Pa) the saturated pressure of water vapor, M_w the molar mass of water, R the constant of perfect gases, and T the temperature.

To compute the advective flow of gaseous air, one needs the gas velocity from Eq. 11 and the density of gaseous air ρ_a^g which varies with the mean gas pressure of the matrix:

$$\rho_a^g = \rho_a^{g,0} \times \left(\frac{P_{g,average}}{P_{g,0}}\right) \tag{15}$$

where $\rho_a^{g,0}$ (kg/m^3) is the initial density of gaseous air, $P_{g,average}$ (Pa) is the mean gas pressure at the macroscale integration point, and $P_{g,0}$ (Pa) is the initial gas pressure inside the porous structure (pressure at which $\rho_a^{g,0}$ was computed).

For the advective flow of dissolved air, one needs the liquid velocity from Eq. 6 and the density of dissolved air ρ_a^l, which is obtained through Henry's law, under the hypothesis that the presence of dissolved air doesn't modify the liquid phase properties:

$$\rho_a^l = H_a(T)\ \rho_a^g \tag{16}$$

with H_a the Henry's constant for air which depends on the temperature.

Finally, the only remaining terms of Eqs. 3 and 4 are the diffusive flow of water vapour, the diffusive flow of dissolved air, and the diffusive flow of the gaseous mix, all expressed by the Fick's second law:

$$i_j^{a,d} = -\rho_w\, S_{r,w}\, n\, \tau\, D_a^{w,l}\, \frac{\partial}{\partial x_j}\left(\frac{\rho_a^w}{\rho_w}\right) \tag{17}$$

$$i_j^{a,g} = -\rho_g\, (1 - S_{r,w})\, n\, \tau\, D_a^{w,g}\, \frac{\partial}{\partial x_j}\left(\frac{\rho_a^g}{\rho_g}\right) = -i_j^{w,g} \tag{18}$$

where n is the porosity and τ the tortuosity, and with ρ_a^w (kg/m^3) the density of dissolved air and $D_a^{w,l} = 2 \times 10^{-9}$ m^2/s the coefficient of diffusion of dissolved air inside liquid water. $D_a^{w,g}$ (m^2/s) is the diffusion coefficient of the dry air inside the water vapour:

$$D_a^{w,g} = D_0 \left(\frac{P_{g,0}}{P_g}\right)\left(\frac{T}{T_0}\right)^{1.75} \tag{19}$$

where $D_0 = 2.42 \times 10^{-5}$ m^2/s, $P_{g,0} = 101325$ Pa and $T_0 = 303$ K.

The Henry's law expresses the equilibrium between dry air in the gas phase and dissolved air in the liquid phase:

$$P_a^l = K_a^l\, x_a^l \tag{20}$$

which formulates that under constant temperature, the molar fraction of dissolved air, noted x_a^l, is proportional to the partial pressure of air through a constant K_a^l.

3.1.2 Mesoscale chloride ingress

The mass balance equation of the chloride ions, in a fixed and undeformable system, is:

$$\frac{\partial}{\partial x_j}(v_j^c) = 0 \tag{21}$$

where v_j^c (m/s) is the chloride flow rate per unit area.

The chlorides flow is the sum of the contribution of the advection, dispersion and diffusion flows [45–49]. The advection flow is due to water flows, while the diffusion flow is due to a gradient of concentration inside the fluid phase. The dispersion flow, finally, is due to the irregularity of the porous system. One can therefore write:

$$\begin{aligned} v_j^c &= v_j^{\text{advection}} + v_j^{\text{diffusion+dispersion}} \\ &= C_M\, v_{j,\text{homogenized}}^l - D_{app}\, \frac{\partial\, C_m}{\partial\, x_j} \end{aligned} \tag{22}$$

where C_M and C_m are, respectively, the concentration in chloride ions at the macroscale and mesoscale integration points, $v_{j,\text{homogenized}}^l$ (m/s) is the homogenized macroscale liquid velocity obtained with Darcy's law (Eq. 6) and D_{app} (m^2/s) is the apparent diffusion and dispersion coefficient, obtained experimentally.

3.1.3 Macroscale mass balance equations

The mass balance equations at the macroscale are similar to the mesoscale ones, with the addition of a storage term. They are shown in Eqs. 23 to 25.

$$\frac{\partial}{\partial x_j}(\rho_w^l\, v_{j,\text{homogenized}}^l + \rho_w^g\, v_{j,\text{homogenized}}^g) + \frac{\partial}{\partial x_j}(i_{j,\text{homogenized}}^{w,g}) + \frac{\partial S_w}{\partial t} = 0 \tag{23}$$

$$\frac{\partial}{\partial x_j}(\rho_a^g\, v_{j,\text{homogenized}}^g + \rho_a^l\, v_{j,\text{homogenized}}^l) + \frac{\partial}{\partial x_j}(i_{j,\text{homogenized}}^{a,d} + i_{j,\text{homogenized}}^{a,g}) + \frac{\partial S_g}{\partial t} = 0 \tag{24}$$

$$\frac{\partial}{\partial x_j}\left(C_M\, v_{j,\text{homogenized}}^l + v_{j,\text{homogenized}}^c\right) + \frac{\partial S_c}{\partial t} = 0 \tag{25}$$

One recognizes the spatial variation of the flow and the temporal variation of the storage, for each species and phase. The homogenized flows are obtained through the numerical spatial homogenization of the mesoscale flows, proportionally to the surface of the RVE. Storage terms are obtained by computing the total mass of each species over the RVE, for each specific time. The advection of chloride ions due to water flows is coupled at the macroscale, based on the homogenized macroscale chloride content at the Gauss point.

3.2 Homogenized macroscale response

At the mesoscale, the hypothesis of steady-state allows the determination of an analytical stiffness matrix, according to a fully coupled FE scheme, with the flows obtained as a solution to the boundary value problem. The mesoscale flows are then numerically homogenized proportionally to the relative area of each mesoscale integration point. Based on those homogenized flows at the

macroscale Gauss point, the macroscale internal fluxes are obtained through a macroscale FE scheme.

However, the transient and highly non-linear problem at the macroscale doesn't permit the obtaining of an analytical stiffness matrix. It was therefore decided to obtain the macroscale elementary stiffness matrix through perturbations [41]: the applied gradients and mean values of water and gas pressure, as well as chloride concentration, are perturbed in sequence, after which the stiffness matrix is computed for the macroscale:

$$K_{i,j} = \frac{\text{Flux}_{i,\text{perturbated}} - \text{Flux}_{i,\text{original}}}{\text{Perturbation}_j} \tag{26}$$

3.3 Modeling the hysteresis of the water retention curve

In this study, the water retention behavior is represented using the empirical model proposed by Van Genuchten (1980) [27] for the primary drying and wetting curves, while the scanning curves associated with hysteresis are described following the approach of Zhou et al. (2012) [50].

Within the framework of the Van Genuchten model, the degree of water saturation is related to suction through the following expression [27]:

$$S_r = S_{res} + (S_{sat} - S_{res})\left(1 + \left(\frac{s}{\alpha}\right)^n\right)^{-m} \quad \text{with} \quad m = 1 - \frac{1}{n} \tag{27}$$

where n is a dimensionless parameter that governs the rate at which the material (de)saturates, while m is another dimensionless parameter controlling the curvature (or slope) of the water retention curve. The third model parameter, α (Pa), represents the air-entry pressure [6]. Additionally, the maximum and residual degrees of saturation, S_{sat} and S_{res}, respectively, as well as the suction s (Pa), are considered in the formulation [21].

In their version of the model, Zhou et al. [50] use an effective saturation degree, defined as:

$$S_e = \frac{S_r - S_{res}}{S_{sat} - S_{res}} \tag{28}$$

In our model, the following assumption has been made:

$$S_{res} = 0 \quad \text{and} \quad S_{sat,w} = S_{sat,d} = 1 \longrightarrow S_e = S_r \tag{29}$$

The expression of the principal boundary curves of Eq. 27 may be rewritten specifically for the drying curve (with the suffix d) or for the wetting curve (with a suffix w):

$$S_{e,d} = S_{res} + (S_{sat} - S_{res})\left[1 + \left(\frac{s}{\alpha_d}\right)^{n_d}\right]^{-m_d} \tag{30}$$

$$S_{e,w} = S_{res} + (S_{sat} - S_{res})\left[1 + \left(\frac{s}{\alpha_w}\right)^{n_w}\right]^{-m_w} \tag{31}$$

The scanning curves of the hysteresis (suffix s) are then defined through the following expression [50]:

$$\frac{\partial S_{e,s}}{\partial s}(\text{w}) = \left(\frac{s_w}{s}\right)^b \left(\frac{\partial S_{e,w}}{\partial s}\right) \text{ with } s_w = \alpha_w \left(S_e^{-1/m_w} - 1\right)^{1/n_w} \tag{32}$$

$$\frac{\partial S_{e,s}}{\partial s}(\text{d}) = \left(\frac{s_d}{s}\right)^{-b} \left(\frac{\partial S_{e,d}}{\partial s}\right) \text{ with } s_d = \alpha_d \left(S_e^{-1/m_d} - 1\right)^{1/n_d} \tag{33}$$

where b is a dimensionless positive fitting parameter. It controls the gradient of the hysteresis curve: the closer it is to null, the more parallel the scanning curve is to the boundary curve. In the opposite, the greater it gets, the more horizontal the scanning curve is [50]. The principal wetting and drying curves, along with a random scanning curve, are represented in Fig. 5.

Finally, the degree of saturation at time t is computed by adding the value at the previous time step, S_e^{t-1}, to the product of the previously defined derivative and the suction increment, ds:

$$S_e^t = S_e^{t-1} + \left(\frac{\partial S_{e,s}}{\partial s}\right)^t ds \tag{34}$$

This formulation highlights that the suction increment has a critical influence on the accuracy of the results, since the scanning curve is derived from the slope of the main boundary curve at a given suction.

4 Experimental results

Table 3 displays a summary of the experimental results obtained on the mortar paste and both natural and recycled concretes. For more details on the experimental methods, see references [6, 33].

If we first look at the dry densities and porosities of our materials, which are obtained based on measurements on 40 samples, it can be seen that the NAC is denser and less porous than the RAC, which is due to the presence of less dense adherent mortar in the RCA, which is relevant with the literature [51–53]. The E-M is slightly less dense and more porous than the RAC. Overall, the greater the volume fraction of mortar in the mix, the less dense and more porous the material is.

With regards to the intrinsic water permeability, which is the mean on four samples, the RAC and the NAC have a similar mean value, although the RAC is slightly more permeable. It is, once again, in accordance with the literature [54]. The E-M, on the other hand, is more than 10 times more permeable, which clearly indicates a more interconnected porous system with larger pores than the

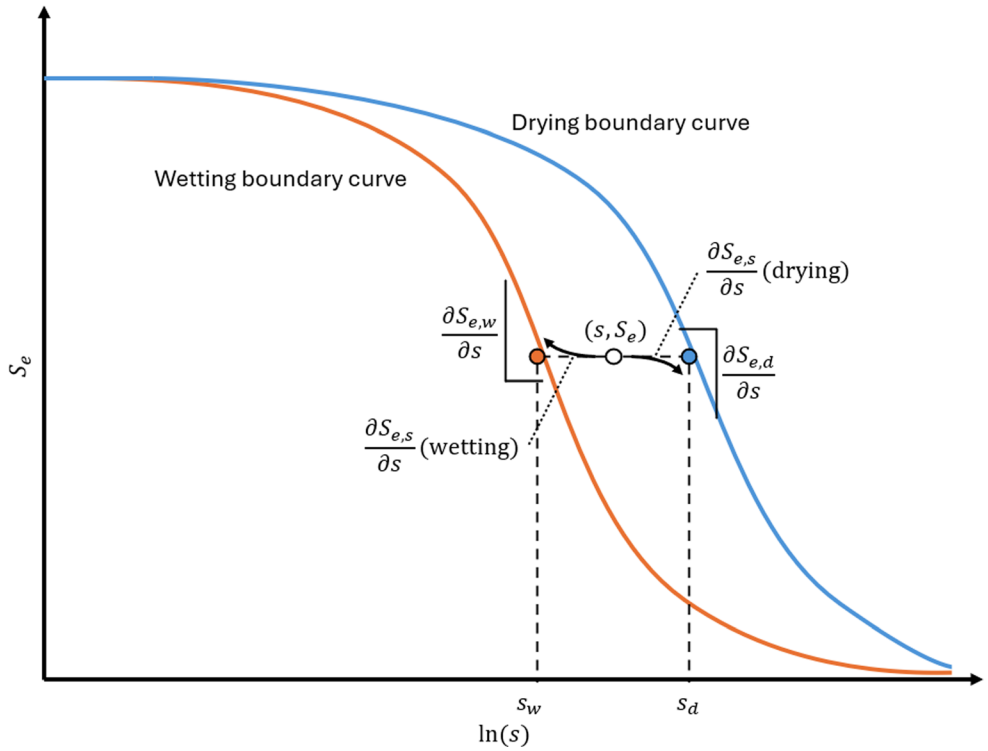

Fig. 5 Drying/wetting boundary and scanning curves (modified after [50])

Table 3 Intrinsic properties of the E-M, NAC, and RAC obtained experimentally and used in the numerical model developed

Variable	NAC	RAC	E-M
Water absorption by immersion			
Dry densities (kg/m^3)	2 263.3 ± 9.4	2 060.7 ± 8.6	2 024.9 ± 5.1
Open porosity (%)	14.16 ± 0.34	20.50 ± 0.29	22.83 ± 0.29
Intrinsic water permeability			
Intrinsic water permeability ($\times 10^{-19}$m^2)	1.73 ± 0.88	2.58 ± 2.61	38.7 ± 20.67
Water retention curves			
n_d	1.39	1.36	1.35
n_w	1.38	1.36	1.4
α_d (MPa)	8.16	7.2	6.23
α_w (MPa)	0.41	0.54	0.77
Hysteresis b_1	0.85	0.75	0.8
Hysteresis b_2	1.2	1.2	1.1
Chloride diffusion under non-steady state			
D_{app} (10^{-12}m^2/s at 29 days)	14.4	16.5	14.3

concrete mixes. The standard deviations presented may seem high but are quite acceptable in spite of the scale used, the three mixes presenting low intrinsic permeabilities compared to the literature. The water retention curves will be discussed in more details thereafter. The last parameter to discuss is therefore the diffusion coefficient under unsteady-state. Theses results are obtained by applying Fick's second law to 8–12 experimental data points, with R^2 ranging from 0.97 to 0.99. The measurements were performed on samples that were immersed in a saline solution for 29 days. All three compositions display a similar diffusion coefficient, with the RAC being slightly more diffusive than the NAC, which corroborates the results found in the literature [52, 55–57].

Figure 6 demonstrates the fitting of our experimental water retention curves with the empirical model by Van Genuchten. The fitted drying and wetting curves are represented in plain and dash lines, respectively. Experimental results are displayed by markers and their corresponding error bars.

Initially, the empirical model by Van Genuchten was developed for granular materials such as soils. Its use in concrete is rather broadly accepted but the introduction of new materials, notably RCA, into concrete, requires a validation of the applicability of this empirical model to RAC.

Based on the fitting performed, it can be concluded that the Van Genuchten model accurately depicts the water retention curve of RAC. Only one experimental point, at high suction during the wetting phase, is not accurately represented, for all compositions. However, high suction is obtained experimentally through the use of silica beads, and the relative humidity associated to them is highly variable, possibly leading to false equilibrium conditions.

If we look at the value of each parameter (Table 3), the one controlling the rate of (de)saturation, n, is similar in drying and wetting for a given composition, while differences in between compositions are also negligible. This was expected as this parameter is dependent on the type of porosity presented: because all our materials are made of the same cement paste, the type of porous structure is similar.

The second parameter, α (Pa), is correlated to the air-entry pressure. This air-entry pressure dictates the necessary applied suction to enter the unsaturated state, both in drying (from gas-saturated to unsaturated) and wetting (from water-saturated to unsaturated). During desorption, a larger maximum pore size is associated with lower values of the parameter α_d, whereas an inverse trend is observed during sorption. Compared to NAC, RAC exhibits a reduced air-entry pressure along the drying path and an increased one during wetting. This behavior suggests that RAC is characterized by a wider pore size distribution, with larger maximum pores and smaller minimum pores than those found in NAC. Overall, this indicates that the RAC will saturate and desaturate sooner than the NAC, for identical applied boundary conditions.

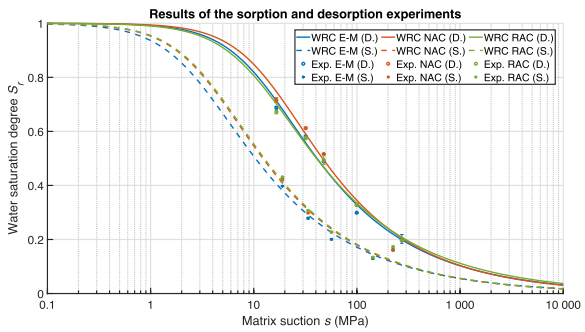

Fig. 6 Experimental wetting and drying data for the three materials considered, together with the corresponding Van Genuchten model fits used to describe their water retention behavior

Figure 7 presents the outcomes of the hysteresis tests. Two distinct hysteretic sequences were investigated. In both cases, the specimens were initially in a fully dry state and subsequently subjected to moisture uptake along the primary wetting curve, followed by three consecutive drying stages, at distinct suction, and a final rewetting phase. Experimental observations are indicated by markers.

The hysteresis formulation proposed by Zhou et al. (2012) [50] was subsequently calibrated using the parameters of the previously identified main boundary curves. Although each hysteresis path led to a different fitted value of the parameter b, the spread between the lowest ($b = 0.75$) and highest ($b = 1.2$) values remains marginal.

5 Sensitivity analysis on the hysteresis

The empirical model implemented to account for the WRC and their hysteresis are based on three parameters: n, α, and b [27, 50]. Another key variable, which is strongly influenced by the boundary conditions, is the suction increment ds. Its value can affect the accuracy of the estimated slope of the scanning curve, as indicated in Eq. 34, resulting in errors.

The first three parameters are determined by fitting the experimental data, although sorption and desorption tests can be time-consuming and labor-intensive, especially when hysteresis effects are being considered. The experimental results showed little deviation for the first two and therefore, a sensitivity analysis on these parameters is not necessary. However, for the third parameter, the experimental results obtained in this study indicate that a single value of b may not adequately represent the same material, as its behavior depends on the material's history. Therefore, it is essential to assess the influence of b on the model's response by performing a sensitivity analysis to evaluate its significance.

The last variable, the suction increment ds, is controlled by the imposed boundary conditions. As per Eq. 34, the derivative $\left(\partial S_{e,s}/\partial_s\right)^t$ is calculated at time t and deemed constant throughout the suction increment ds: the model is therefore prone to error for large increments.

The two following sections investigate the influence of the variables described above. The numerical model relies on the parameters presented in Table 3.

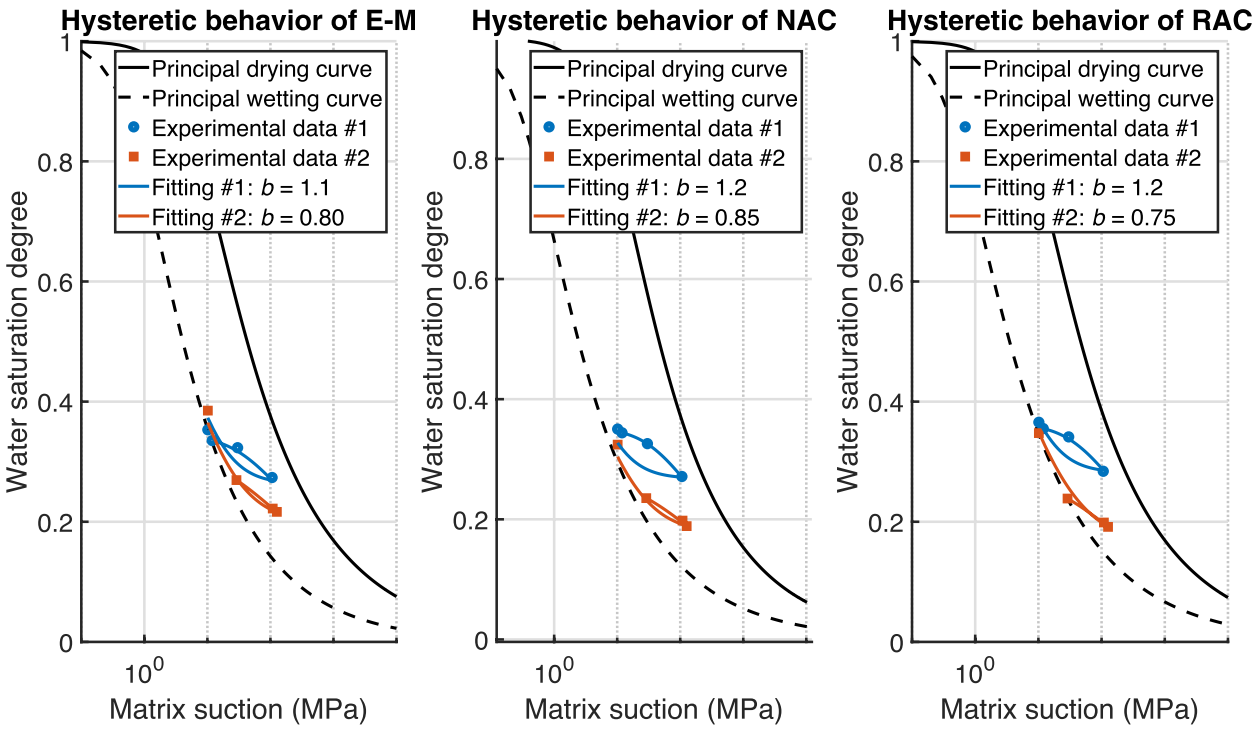

Fig. 7 Representation of the water retention hysteresis for the three materials, reproduced using the model proposed by Zhou et al. (2012) [50]

Since the mesoscale is mainly filled with permeable mortar, the mesoscale properties implemented in the simulations (namely porosity, intrinsic water permeability, and chloride diffusion coefficient) are based on the E-M material and corrected by a factor of 1.3 to account for the transition from a 2D representation to a 3D reality [39, 58]. This correction was validated through reverse modeling of experiments, and is explained by the lack of out-of-plane flow in 2D.

In contrast, the WRC is treated as a macroscale property, since its parameters are primarily determined by the pore type and size. In the multiscale model, these fine-scale features are not explicitly represented, making homogenization necessary. Two approaches were considered: either defining the WRC as a mesoscale property, using the parameters associated with the E-M composition, or treating them as a macroscale property and directly employing the parameters measured for the concrete. The latter approach was adopted, as the former was deemed to oversimplify the problem. Consequently, the WRC parameters implemented correspond to either NAC or RAC, depending on the material under consideration.

In the following, only the RAC will be studied: Fig. 8 shows the mesoscale representative volume element

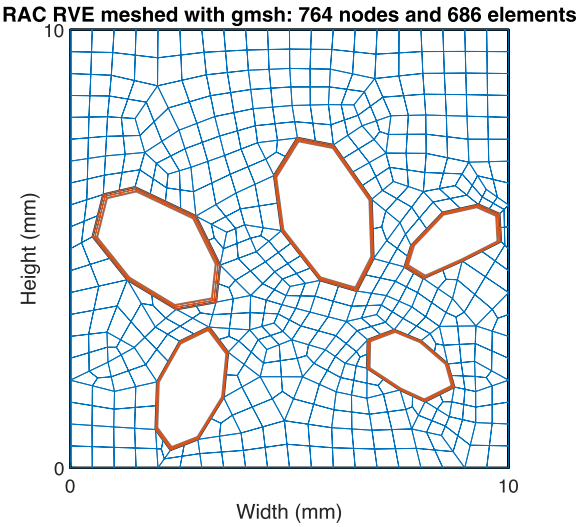

Fig. 8 Representative volume element of the RAC mesoscale, where the blue phase corresponds to the new mortar matrix and the orange phase to the adhered mortar of the recycled aggregates. Both phases are assigned the material properties of the E-M composition. The size of the RVE was chosen on the smaller size to limit computation time associated with the sensitivity analysis while maintaining accurate results

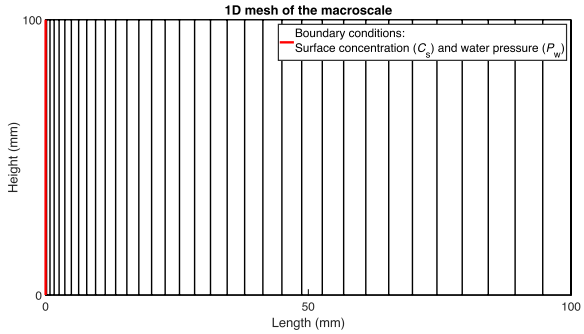

Fig. 9 Macroscale mesh used to investigate the influence of the suction increment *ds* and the parameter *b* on the hysteresis model. Boundary conditions, in the form of imposed water pressure and chloride concentration, are imposed on the left border. The mesh is chosen to be more refined closer to the boundary conditions

modeled. The macroscale represents a 1D sample that is 10 cm long (Fig. 9), imposed on the left border.

5.1 Influence of the increment of suction

Concrete elements are subjected to relative humidity and temperature change throughout their lifetime. When modelling theses solicitations, it is common to impose a varying suction as boundary condition. As per Eq. 34, the calculation of the saturation degree depends on the increment of suction applied and on the value of $\left(\partial S_{e,s}/\partial_s\right)^t$, by making the hypothesis that this gradient of saturation is constant over the increment *ds*. For large time step, the increment of suction may therefore be large and lead to errors on the saturation degree. To decrease the numerical error, one option could be to limit the maximum time step of our simulation. However, this would greatly increase the computation time necessary. Another possible option is to implement an integrative approach to Eq. 34:

$$S_e^t = S_e^{t-1} + \sum_{i=1}^{N} \left(\frac{\partial S_{e,s}}{\partial s} \right)^{t_i} \times \min\left(ds_{max}, ds\right) \qquad (35)$$

where N is the number of sub-increments. It is calculated through $N = ds/ds_{max}$, where ds_{max} is a maximum increment of suction to be imposed. Finally, the time t_i is equal to $(t-1) + i\ (\Delta t/N)$.

A sensitivity analysis was therefore performed with our FE^2 model, in order to determine the maximum value of that sub-increment.

The results are presented in Fig. 10, which illustrates the model responses obtained for four different values of $ds_{\max}$: the suction increment prescribed by the boundary

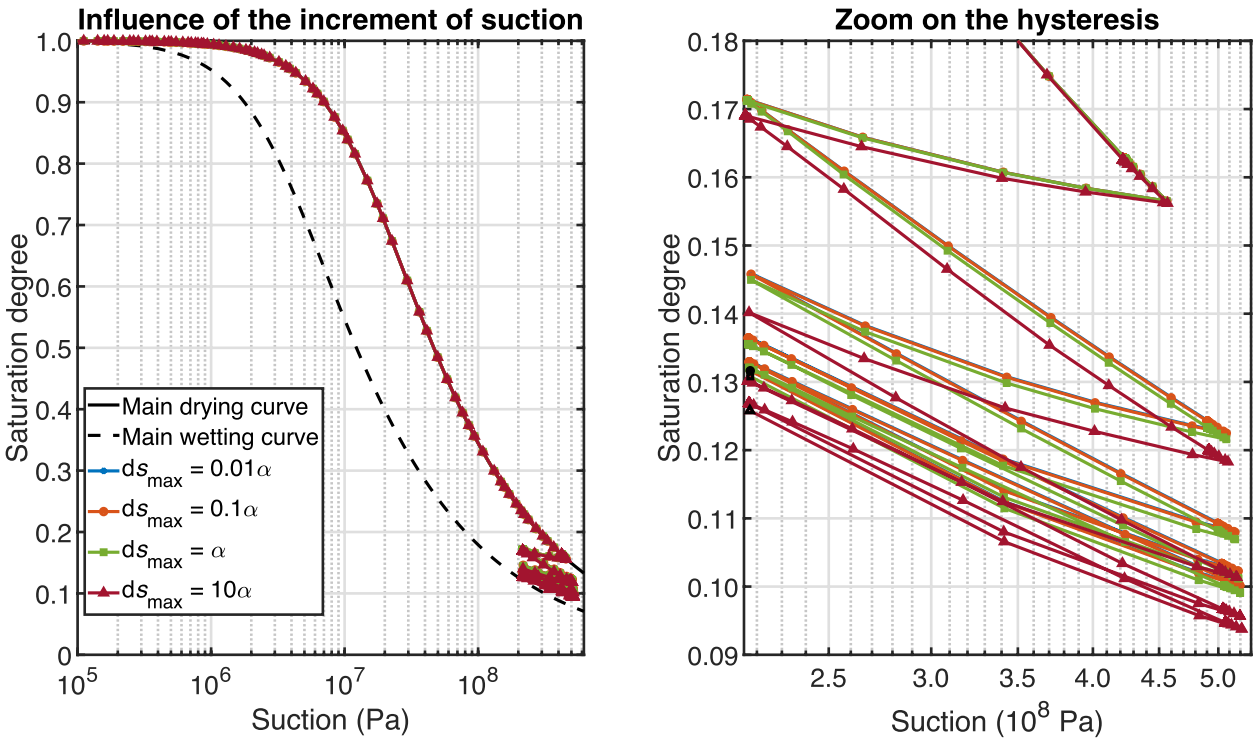

Fig. 10 Influence of the suction increment on the hysteresis model. Left: overall model response for four different suction increments ($ds_{\max}$ (Pa)). Right: detailed view highlighting the hysteresis behavior. The term α (Pa) represents the value of the parameter related to the air-entry pressure of the material studied, as per Van Genuchten

conditions is subdivided into equal sub-steps of magnitude $ds_{\max}$ (Pa). The level of discretization in the suction increments influences the computed degree of saturation, even under identical final suction conditions. Depending on the selected value of $ds_{\max}$, these discrepancies can be substantial.

In order to maintain a physical meaning to ds_{max}, it was decided to correlate its value to the Van Genuchten parameter α. Based on the obtained results, it can be concluded that the maximum value of ds_{max} is strictly equal or inferior to the value of 0.1α, to remain accurate.

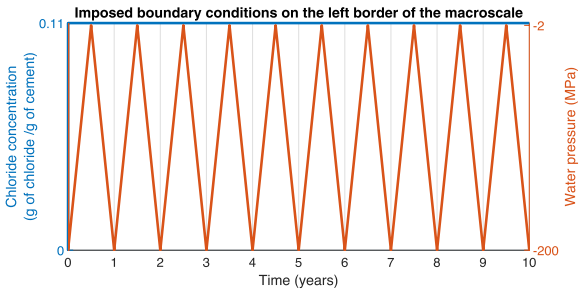

Fig. 11 Boundary conditions imposed on the left border of the macroscale mesh (represented in Fig. 9) for the parametric study of parameter *b* on the results of the model

5.2 Influence of parameter *b*

The second parameter investigated is b, a positive, dimensionless variable that governs the slope of the hysteresis scanning curve. Depending on its value, this curve can vary from being nearly parallel to the main water retention curve (for b approaching zero) to almost horizontal (for large values of b). Experimental observations indicate that, for a given material, the value of b is not constant but depends on its water exchange history. A sensitivity analysis is therefore required in order to measure the influence of this variability. When modeling WRC, several options are available:

- Modeling a single boundary curve, in wetting or drying, depending on the dominating phenomenon to be studied;
- Modeling a single boundary curve with mean properties between the wetting and drying one;
- Modeling the two boundary curves and their hysteresis.

For the last option, the value b is to be calibrated experimentally.

In the following, all three options will be studied, with the addition of several values for the parameter b in the third option. As for the previous section, only the RAC will be studied.

In theses simulations, the initial water pressure inside the sample is equal to the atmospheric pressure. The pressure applied on the left exterior boundary is alternated every six months between −2 MPa and −200 MPa over a period of ten years. In addition, the left boundary is prescribed a chloride concentration of 0.11 g Cl^-/g cement, while the interior of the sample is initially free of chloride. The macroscale mesh and the corresponding boundary conditions are illustrated in Figs. 9 and 11, respectively.

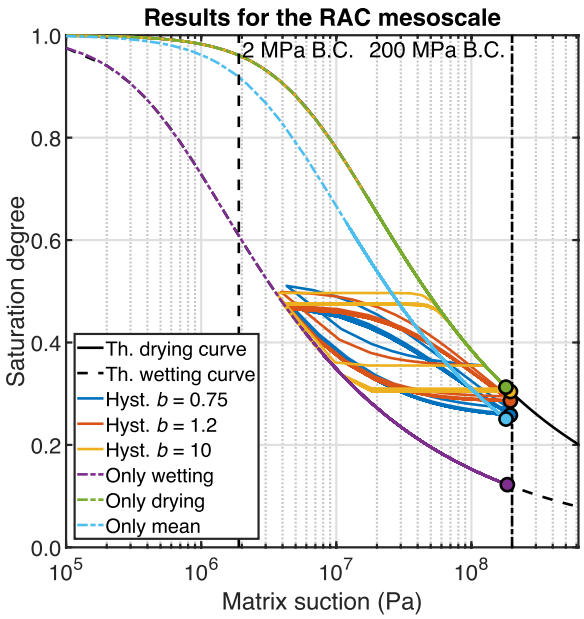

Fig. 12 Influence of the parameter *b* on the hysteresis model: evolution of the saturation degree with the applied suction for RAC. The two black curves are the theoretical boundary curves in wetting and drying. Three distinct values of *b* are defined for the hysteresis model (blue, orange, and yellow). Three more curves are obtained without the hysteresis model, with parameters of the main boundary curves only (purple and green), or a mean set of parameters (light blue). Finally, the two boundary conditions (B.C.) are defined vertically. The last point of the simulation is represented with a large colored dot marker. Results are shown at the first Gauss point of the first element, explaining the small discrepancy between the last result of the simulations and the boundary conditions

Figure 12 displays the results of our multiscale model for a RAC RVE. The two black curves are the theoretical boundary curves in wetting and drying. Three distinct values of b are defined for the hysteresis model (blue, orange, and yellow). Three more curves are obtained without the hysteresis model, with parameters

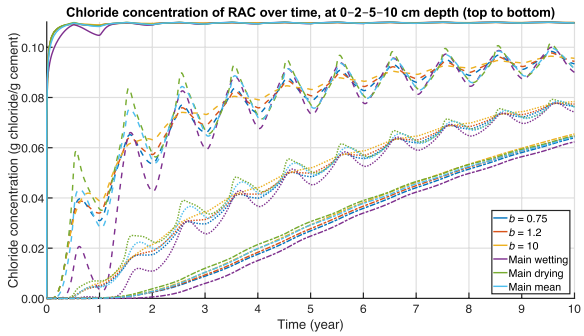

Fig. 13 Effect of the fitting parameter *b* on the hysteresic model: ten-years temporal evolution of chloride content (g chloride/g cement) in the RAC at depths of 0, 2, 5, and 10 cm (top to bottom)

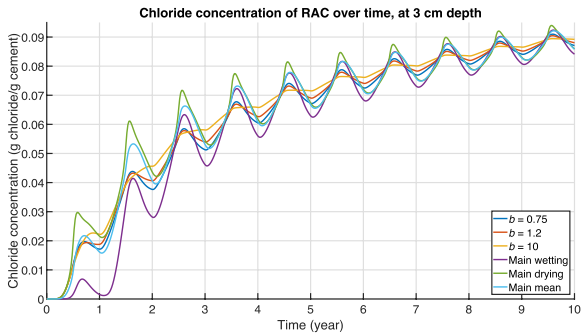

Fig. 14 Effect of the fitting parameter *b* on the hysteresic model: ten-year temporal evolution of chloride content (g chloride/g cement) in the RAC at 3 cm depth

of the main boundary curves only (purple and green), or a mean set of parameters (lightblue). Finally, the two boundary conditions are defined vertically.

As per its definition, the higher the value of *b*, the more horizontal the scanning curves are, meaning that they reach the boundary curves faster. One may see, thanks to the colored dot markers, that the use of the hysteresis and the use of a correct value of *b* has a great incidence on the last result of our simulations.

Chloride ingress is closely linked to the saturation degree of concrete, as the relative contribution of transport mechanisms (diffusion versus advection) depends on the local water content. The hysteresis model parameter *b* affects the shape of the wetting-drying scanning curves, and consequently the saturation degree at a given capillary pressure. Different values of *b* therefore alter the distribution of water within the concrete, which in turn modulates the dominant transport mechanism. In other words, *b* indirectly influences long-term chloride ingress, which makes the study of chloride ingress a great indicator of the effects of *b* on our model. Figure 13 depicts the temporal evolution of chloride content within the RAC sample at depths of 0 cm, 2 cm, 5 cm, and 10 cm (from top to bottom) over a ten-year period. For clarity, Fig. 14 presents the results at a single depth of 3 cm only.

Firstly, a clear trend emerges: in the zone where wetting and drying cycles are most prevalent, chloride content differences are the greatest. Based on the main sources of chloride ingress (advection due to water flows and diffusion), it is expected that the greater the water content, the greater the diffusion, and the greater the amplitude of the water flows, the greater the advection.

For simulations with only one defined curve, using the main wetting curve leads to a smaller saturation degree at equal suction. This, in turn, leads to an overall smaller chloride content at all time. For the boundary curve in drying, it is the opposite. However, for the mean boundary curve, the chloride content is closer to the main drying curve than to the wetting boundary curve.

For simulations with hysteresis implemented, it can be concluded that the greater the value of *b*, the smaller the variations between the drying and wetting phases. As a result, the water saturation degree changes more gradually, leading to higher chloride concentrations for larger values of *b*, although the differences between the three values represented are negligible. In the absence of an experimental campaign, employing a larger *b* value is considered conservative, since it leads to an overestimation of the chloride concentration.

Another observation is that at larger depths, the effect of the boundary conditions is reduced because chloride migration is primarily controlled by diffusion, with advection playing a minor role. The unsaturated front is thus less pronounced. Near the exposed surface, the effect of varying *b* is minimal, as the imposed boundary conditions dominate the response.

Based on Figs. 13 and 14, it can be concluded that implementing the hysteresis of the water retention curve is necessary for accurately depicting chloride ingress in unsaturated concrete. It is also preferable, though not essential, to employ the appropriate value of *b*, determined experimentally, in order to avoid overpredicting the chloride content inside the sample.

However, Fig. 15 shows that the difference in chloride content decreases greatly over time. This figure relates the mean chloride content inside the first 2 cm of the RAC at 190 and 3 650 days of simulation. Indeed, after 10 years, only a slight difference in the mean chloride content for different values of *b* is visible. As degradation reactions are long-term rather than short-term processes, it could be concluded that the hysteresis of the WRC could be neglected on an industrial scale in order to simplify models and decrease simulation time.

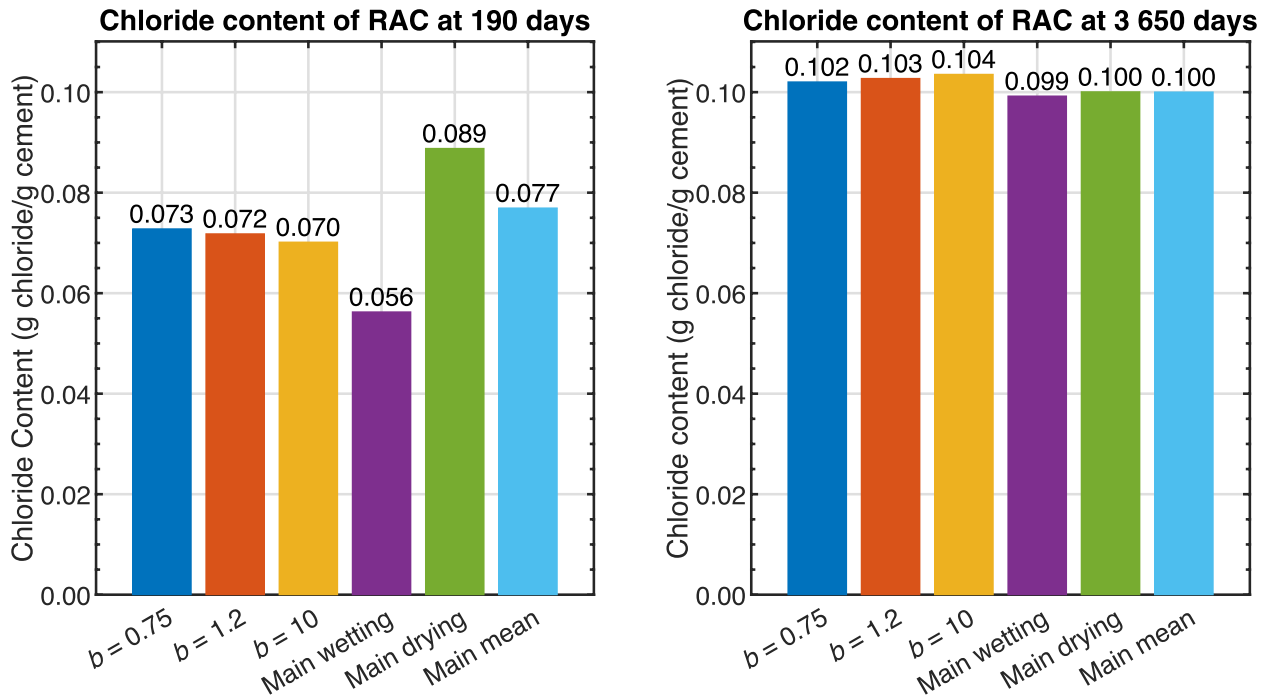

Fig. 15 Effect of the fitting parameter b on the hysteresic model: mean chloride content over the first 2 cm of the sample, after 190 and 3 650 days

6 Conclusions

This work implemented a hysteresis-based model for the water retention curves of RAC, combining the Van Genuchten boundary curves [27] and the hysteresis formulation of Zhou et al. [50]. Both models were calibrated using experiments conducted on (NAC, RAC, and a mortar (E-M).

The results confirm that the Van Genuchten model is suitable for mortar and concretes, including RAC. The hysteresis tests showed that the parameter b varies with the material's history, motivating a sensitivity analysis. A second sensitivity analysis concerned the suction increment ds (Eq. 34), which proved influential and required the use of sub-increments limited by the Van Genuchten parameter α.

Numerical FE^2 simulations demonstrated that higher b values yield higher chloride contents and smaller fluctuations in water saturation degree. For long-term degradation scenarios involving chloride ingress, hysteresis effects become less significant, suggesting that hysteresis may be neglected in industrial applications without major loss of accuracy, although it remains valuable for scientific precision. However, the effect of hysteresis on other long-term mechanisms (carbonation, freeze-thaw cycles) still needs to be investigated. Furthermore, long-term effects may modify the microstructure of concrete, resulting in modifications of the water retention curves. This phenomenon is under investigation.

Experimentally, RAC exhibited lower air-entry pressure during drying and higher during wetting than NAC, indicating earlier moisture exchange with the environment. Both materials showed similar values of the parameter n, which corresponds to the rate of exchange. Their chloride profiles confirmed higher chloride ingress in RAC, consistent with its greater moisture exchange and diffusion coefficient.

Authors' contributions

Arthur Fanara: Writing – original draft, Validation, Project administration, Methodology, Investigation, Funding acquisition, Formal analysis. Luc Courard: Writing – review & editing, Validation, Supervision, Resources, Project administration, Funding acquisition, Conceptualization. Frédéric Collin: Writing – review & editing, Validation, Supervision, Software, Resources, Project administration, Methodology, Funding acquisition, Conceptualization.

Funding

This work is supported by the Wallonia regional government (Belgium) in the framework of a FRIA (Fund for Industrial and Agricultural Research) grant.

Data availability

Experimental and numerical data obtained during the current study are available upon reasonable request from the corresponding author. Access to the modeling software used is restricted to partnership institutions.

Declarations

Competing interests

The authors declare that they have no known competing financial interests or personal relationships that could have appeared to influence the work reported in this paper.

Received: 24 November 2025 Revised: 23 February 2026 Accepted: 22 April 2026
Published online: 09 May 2026

References

1. CEMBUREAU. (2021). *European Cement Association: Activity Report 2020*. Technical report.
2. Pacheco, J. N., de Brito, J., & Tornaghi, M. L. (2023). *Use of recycled aggregates in concrete: opportunities of upscaling in Europe*. JRC131294. Publications Office of the European Union, Luxembourg. https://doi.org/10.2760/144802
3. UEPG. (2021). *European Aggregates Association: Annual Review 2020–2021*. Technical report.
4. EUROSTAT (2023). ENV_WAS: European statistics on waste. Technical report.
5. Debieb, F., Courard, L., Kenai, S., & Degeimbre, R. (2010). Mechanical and durability properties of concrete using contaminated recycled aggregates. *Cement & Concrete Composites, 32*, 421–426. https://doi.org/10.1016/j.cemconcomp.2010.03.004
6. Fanara, A., Courard, L., Collin, F., & Hubert, J. (2022). Transfer properties in recycled aggregates concrete: Experimental and numerical approaches. *Construction and Building Materials, 326*, Article 126778. https://doi.org/10.1016/j.conbuildmat.2022.126778
7. Rao, A., Jha, K. N., & Misra, S. (2007). Use of aggregates from recycled construction and demolition waste in concrete. *Resources, Conservation and Recycling, 50*, 71–87. https://doi.org/10.1016/j.resconrec.2006.05.010
8. Rangel, C. S., Amario, M., Pepe, M., Martinelli, E., & Toledo Filho, R. D. (2020). Influence of wetting and drying cycles on physical and mechanical behavior of recycled aggregate concrete. *Materials, 13*(24), Article 5675. https://doi.org/10.3390/ma13245675
9. Mangat, P. S., & Molloy, B. T. (1994). Prediction of long term chloride concentration in concrete. *Materials and Structures, 27*, 338–346. https://doi.org/10.1007/bf02473426
10. Patel, R. A., Janez, P., & Diederik, J. (2017). Multi-scale modeling strategies to improve durability models for service life predictions of concrete structures. In Schutter, G. D., Belie, N. D., Janssens, A., and Bossche, N. V. D., (Eds.), *XIV DBMC - 14th International Conference on Durability of Building Materials and Components* (pp. 309–310). Ghent University, Belgium. RILEM.
11. Morga, M., & Marano, G. C. (2015). Chloride penetration in circular concrete columns. *International Journal of Concrete Structures and Materials, 9*(2), 173–183. https://doi.org/10.1007/s40069-014-0095-y
12. Balafas, I., & Burgoyne, C. J. (2010). Environmental effects on cover cracking due to corrosion. *Cement and Concrete Research, 40*, 1429–1440. https://doi.org/10.1016/j.cemconres.2010.05.003
13. Bear, J., & Verruijt, A. (1987). *Modeling Groundwater Flow and Pollution*. Springer.
14. Beckett, C. T., & Augarde, C. E. (2013). Prediction of soil water retention properties using pore-size distribution and porosity. *Canadian Geotechnical Journal, 50*(4), 435–450. https://doi.org/10.1139/cgj-2012-0320
15. Nuth, M., & Laloui, L. (2008). Advances in modelling hysteretic water retention curve in deformable soils. *Computers and Geotechnics, 35*(6), 835–844. https://doi.org/10.1016/j.compgeo.2008.08.001
16. Pap, M., Mahler, A., & Nehme, S. G. (2018). Measurement of water retention curve for different concrete mixtures. TC106 Conferences in Unsaturated Soils - 7th International Conference on Unsaturated Soils 2018, Hong Kong.
17. Pham, H. Q., Fredlund, D. G., & Barbour, S. L. (2005). A study of hysteresis models for soil-water characteristic curves. *Canadian Geotechnical Journal, 42*(6), 1548–1568. https://doi.org/10.1139/t05-071
18. Bowen, R. M. (1980). Incompressible porous media models by use of the theory of mixtures. *International Journal of Engineering Science, 18*, 1129–1148. https://doi.org/10.1016/0020-7225(80)90114-7
19. Concha, F. A. (2014). Solid-Liquid Separation in the Mining Industry, volume Fluid Mechanics and Its Applications (Book 105). *Springer International Publishing Switzerland*. https://doi.org/10.1007/978-3-319-02484-4
20. Pap, M., Mahler, A., & Nehme, S. G. (2018). Analysis and finite element modelling of water flow in concrete. *Periodica Polytechnica Civil Engineering*. https://doi.org/10.3311/PPci.13005
21. Fredlund, D. G., Sheng, D., & Zhao, J. (2011). Estimation of soil suction from the soil-water characteristic curve. *Canadian Geotechnical Journal, 48*, 186–198. https://doi.org/10.1139/t10-060
22. Capparelli, G., & Spolverino, G. (2020). An empirical approach for modeling hysteresis behavior of pyroclastic soils. *Hydrology, 7*(1), Article Article 14. https://doi.org/10.3390/hydrology7010014
23. Likos, W. J., Lu, N., & Godt, J. W. (2014). Hysteresis and uncertainty in soil water-retention curve parameters. *Journal of Geotechnical and Geoenvironmental Engineering*. https://doi.org/10.1061/(asce)gt.1943-5606.0001071
24. Abbasi, F., Javaux, M., Vanclooster, M., & Feyen, J. (2012). Estimating hysteresis in the soil water retention curve from monolith experiments. *Geoderma, 189–190*, 480–490. https://doi.org/10.1016/j.geoderma.2012.06.013
25. Simunek, J., Kodesova, R., Gribb, M. M., & van Genuchten, M. T. (1999). Estimating hysteresis in the soil water retention function from cone permeameter experiments. *Water Resources Research, 35*(5), 1329–1345. https://doi.org/10.1029/1998wr900110
26. Kohgo, Y. (2008). A hysteresis model of soil water retention curves based on bounding surface concept. *Soils and Foundations, 48*(5), 633–640. https://doi.org/10.3208/sandf.48.633
27. Van Genuchten, M. T. (1980). A closed-form equation for predicting the hydraulic conductivity of unsaturated soils. *Soil Science Society of America Journal, 44*(892), Article Article 898. https://doi.org/10.2136/sssaj1980.03615995004400050002x
28. Jiménez, A. M. G., de Farias, M. M., Neto, M. P. C., & Calle, I. F. O. (2014). Water retention curve and particle breakage of aggregates recycled from demolition waste. *Journal of Civil Engineering and Architecture, 8*(9). https://doi.org/10.17265/1934-7359/2014.09.013
29. Tong, L.-Y., Xiong, Q. X., Ke, X., Alderete, N. M., De Belie, N., & Liu, Q.-F. (2025). Advanced modelling of moisture transport process in unsaturated cementitious materials considering multi-modal pore size distributions. *Cement and Concrete Research, 198*, Article 107973. https://doi.org/10.1016/j.cemconres.2025.107973
30. Hubert, J., Zhao, Z., Michel, F., & Courard, L. (2023). Effect of crushing method on the properties of produced recycled concrete aggregates. *Buildings, 13*(9), Article 2217. https://doi.org/10.3390/buildings13092217
31. Zhao, Z., Xiao, J., Damidot, D., Rémond, S., Bulteel, D., & Courard, L. (2022). Quantification of the hardened cement paste content in fine recycled concrete aggregates by means of salicylic acid dissolution. *Materials, 15*(9), Article 3384. https://doi.org/10.3390/ma15093384
32. Schwartzentruber, A., & Catherine, C. (2000). La méthode du mortier de béton équivalent (MBE) - Un nouvel outil d'aide à la formulation des bétons adjuvantés. *Materials and Structures, 33*(8), 475–482. https://doi.org/10.1007/bf02480524
33. Fanara, A., Courard, L., & Collin, F. (2023). Numerical and experimental study of chloride ion transport in recycled aggregates concrete. *Academic Journal of Civil Engineering, 40*(2), 40–220222022. https://doi.org/10.26168/ajce.40.2.17
34. International Organization for Standardization. (2019). *Geotechnical Investigation and Testing – Laboratory Testing of Soil – Part 11: Determination of Permeability by Constant and Falling Head* (ISO 17892-11: 2019). International Organization for Standardization.
35. NBN (2015). *Testing Hardened Concrete – Part 11: Determination of the Chloride Resistance of Concrete by Unidirectional Diffusion* (NBN EN 12390-11). NBN.
36. Kowalski, S. J. (2003). *Thermomechanics of Drying Processes*. Springer. https://doi.org/10.1007/978-3-540-36405-4
37. Delage, P., Howat, M., & Cui, Y. (1998). The relationship between suction and swelling properties in a heavily compacted unsaturated clay. *Engineering Geology, 50*, 31–48. https://doi.org/10.1016/s0013-7952(97)00083-5

38. Collin, F., Li, X., Radu, J., & Charlier, R. (2002). Thermo-hydro-mechanical coupling in clay barriers. *Engineering Geology, 64*, 179–193. https://doi.org/10.1201/9781003078487-64
39. Fanara, A., Courard, L., & Collin, F. (2024). Numerical FE^2 study of chloride ingress in unsaturated recycled aggregates concrete. *Cement and Concrete Research, 186*, Article 107703. https://doi.org/10.1016/j.cemconres.2024.107703
40. Bertrand, F., Buzzi, O., Bésuelle, P., & Collin, F. (2020). Hydro-mechanical modelling of multiphase flowin naturally fractured coalbed using a multiscale approach. *Journal of Natural Gas Science and Engineering, 78*, Article 103303. https://doi.org/10.1016/j.jngse.2020.103303
41. Marinelli, F., van den Eijnden, A., Sieffert, Y., Chambon, R., & Collin, F. (2016). Modeling of granular solids with computational homogenization: Comparison with Biot's theory. *Finite Elements in Analysis and Design, 119*, 45–62. https://doi.org/10.1016/j.finel.2016.05.003
42. Nilenius, F., Larsson, F., Lundgren, K., & Runesson, K. (2014). FE^2 method for coupled transient diffusion phenomena in concrete. *Journal of Engineering Mechanics, 141*(2), Article 04014110. https://doi.org/10.1061/(ASCE)EM.1943-7889.0000684
43. Kouznetsova, V., Brekelmans, W. A. M., & Baaijens, F. P. T. (2001). An approach to micro-macro modeling of heterogeneous materials. *Computational Mechanics, 27*, 37–48. https://doi.org/10.1007/s004660000212
44. Smit, R. J. M., Brekelmans, W. A. M., & Meijer, H. E. H. (1998). Prediction of the mechanical behavior of nonlinear heterogeneous systems by multi-level finite element modeling. *Computer Methods in Applied Mechanics and Engineering, 155*, 181–192. https://doi.org/10.1016/s0045-7825(97)00139-4
45. Ababneh, A., Benboudjema, F., & Xi, Y. (2003). Chloride penetration in non-saturated concrete. *Journal of Materials in Civil Engineering, 15*(2), 183–191. https://doi.org/10.1061/(asce)0899-1561(2003)15:2(183)
46. Biver, P. (1993). *Phenomenal and Numerical Study on the Propagation of Misicible Pollutants in a Medium with Multiple Porosity* [Unpublished doctoral dissertation]. University of Liège.
47. Liu, Q., Easterbrook, D., Yand, J., & Li, L. (2015). A three-phase, multi-component ionic transport model for simulation of chloride penetration in concrete. *Engineering Structures, 86*, 122–133. https://doi.org/10.1016/j.engstruct.2014.12.043
48. Nagesh, M., & Bhattacharjee, B. (1998). Modeling of chloride diffusion in concrete and determination of diffusion coefficients. *ACI Materials Journal, 95*(2), 113–120.
49. Wu, L., Li, W., & Yu, X. (2017). Time-dependent chloride penetration in concrete in marine environments. *Construction and Building Materials, 152*, 406–413. https://doi.org/10.1016/j.conbuildmat.2017.07.016
50. Zhou, A.-N., Sheng, D., Sloan, S. W., & Gens, A. (2012). Interpretation of unsaturated soil behaviour in the stress - Saturation space, I: Volume change and water retention behaviour. *Computers and Geotechnics, 43*, 178–187. https://doi.org/10.1016/j.compgeo.2012.04.010
51. Limbachiya, M. C., Leelawat, T., & Dhir, R. K. (2000). Use of recycled concrete aggregate in high-strength concrete. *Materials and Structures, 33*(9), 574–580. https://doi.org/10.1007/bf02480538
52. Pedro, D., de Brito, J., & Evangelista, L. (2014). Performance of concrete made with aggregates recycled from precasting industry waste: Influence of the crushing process. *Materials and Structures, 48*(12), 3965–3978. https://doi.org/10.1617/s11527-014-0456-7
53. Thomas, C., Setien, J., Polanco, J., Alaejos, P., & Sanchez de Juan, M. (2013). Durability of recycled aggregate concrete. *Construction and Building Materials, 40*, 1054–1065. https://doi.org/10.1016/j.conbuildmat.2012.11.106
54. Zaharieva, R., Buyle-Bodin, F., Skoczylas, F., & Wirquin, E. (2003). Assessment of the surface permeation properties of recycled aggregate concrete. *Cement and Concrete Composites, 25*(2), 223–232. https://doi.org/10.1016/s0958-9465(02)00010-0
55. Gonzalez, A., & Etxeberria, M. (2014). Experimental analysis of properties of high performance recycled aggregate concrete. *Construction and Building Materials, 52*, 227–235. https://doi.org/10.1016/j.conbuildmat.2013.11.054
56. Russo, N., & Lollini, F. (2022). Effect of carbonated recycled coarse aggregates on the mechanical and durability properties of concrete. *Journal of Building Engineering, 51*, Article 104290. https://doi.org/10.1016/j.jobe.2022.104290
57. Xuan, D., Zhan, B., & Poon, C. S. (2017). Durability of recycled aggregate concrete prepared with carbonated recycled concrete aggregates. *Cement and Concrete Composites, 84*, 214–221. https://doi.org/10.1016/j.cemconcomp.2017.09.015
58. Nilenius, F., Larsson, F., Lundgren, K., & Runesson, K. (2013). *A 3D/2D Comparison between Heterogeneous Mesoscale Models of Concrete* (pp. 249–259). Springer Netherlands. https://doi.org/10.1007/978-94-007-6878-9_18

Publisher's Note